Ruan *et al. Energy Mater.* **2025**, *5*, 500066
DOI: 10.20517/energymater.2024.217

Energy Materials

Article

Open Access

Check for updates

Innovative approaches of porous carbon materials derived from energy waste and their electrochemical properties

Shuai Ruan[1,2], Xinping He[2,*], Hui Huang[2], Yongping Gan[2], Yang Xia[2], Jun Zhang[2], Wangjun Wan[3], Chen Wang[3], Xinhui Xia[2,4,*], Wenkui Zhang[1,2,*]

[1]Moganshan Institute ZJUT, Kangqian District, Deqing 313200, Zhejiang, China.
[2]College of Materials Science and Engineering, Zhejiang University of Technology, Hangzhou 310014, Zhejiang, China.
[3]Zhejiang Academy of Science and Technology for Inspection & Quarantine, Hangzhou 311215, Zhejiang, China.
[4]School of Materials Science and Engineering, Zhejiang University, Hangzhou 310027, Zhejiang, China.

***Correspondence to:** Prof. Xinhui Xia, Science and Engineering, Zhejiang University of Technology, 18 Chaowang Road, Hangzhou 310014, Zhejiang, China. E-mail: cmxwy@zjut.edu.cn; Prof. Xinping He, Science and Engineering, Zhejiang University of Technology, 18 Chaowang Road, Hangzhou 310014, Zhejiang, China. E-mail: xinpinghe@zjut.edu.cn; Prof. Wenkui Zhang, Science and Engineering, Zhejiang University of Technology, 18 Chaowang Road, Hangzhou 310014, Zhejiang, China. E-mail: msechem@zjut.edu.cn

How to cite this article: Ruan, S.; He, X.; Huang, H.; Gan, Y.; Xia, Y.; Zhang, J.; Wan, W.; Wang, C.; Xia, X.; Zhang, W. Innovative approaches of porous carbon materials derived from energy waste and their electrochemical properties. *Energy Mater.* **2025**, *5*, 500066. https://dx.doi.org/10.20517/energymater.2024.217

Received: 17 Oct 2024 **First Decision:** 14 Nov 2024 **Revised:** 27 Nov 2024 **Accepted:** 3 Dec 2024 **Published:** 6 Mar 2025

Academic Editor: Ho Seok Park **Copy Editor:** Fangling Lan **Production Editor:** Fangling Lan

Abstract

The pathway to sustainable development and carbon neutrality is contingent upon the development of high-performance porous carbon electrode materials sourced from biomass and industrial waste. The present research introduces an innovative approach for the fabrication of porous carbon, harnessing the collaborative impact of various materials to transform biomass in the form of corncobs and industrial byproduct fly ash into tiered porous carbon characterized by a high specific surface area and excellent functionality, via a simple hydrothermal activation method. This material is particularly well-suited for applications in supercapacitors, lithium-ion batteries, and other energy storage systems. The porous carbon material fabricated from these two waste streams boasts a wealth of pores and an exceptional specific surface area (1,768 $m^2 g^{-1}$), which in turn confers superior electrochemical performance. The material achieves a remarkable specific capacitance of up to 240 F g^{-1} (at 1 A g^{-1}), and demonstrates remarkable properties for lithium storage. Lithium-ion batteries constructed with this material feature an extensive potential range, with an initial specific capacity of 160 mAh g^{-1} at 0.1 A g^{-1}, and a near-perfect coulomb efficiency of approximately 100%. This research uncovers a novel paradigm for the preparation of

high-performance porous carbon electrode materials through a low-carbon and environmentally conscious approach. It not only advances the pursuit of carbon neutrality and the realization of carbon peak objectives but also underscores the potential of valorizing biomass and industrial byproducts in the context of cutting-edge energy storage technologies.

Keywords: Biomass carbon, fly ash, porous carbon, supercapacitor, lithium-ion battery

INTRODUCTION

Global warming is a result of climate change driven by human energy consumption and the release of significant carbon dioxide emissions, adversely affecting lives and leading to mounting issues. In 2020, China introduced its goals of carbon peaking and neutrality at the UN General Assembly. Subsequently, the nation outlined five key strategies, which include enhancing energy efficiency and establishing a green, low-carbon circular economy. Many fossil fuels are not fully converted during use, leaving byproducts rich in unburned carbon that can harm the environment. Thus, the path to carbon neutrality involves repurposing energy waste into advanced energy storage components for sustainable energy cycles[1-3].

Supercapacitors (SCs) are energy storage devices that operate on the principle of electrochemical conversion, offering quick charge-discharge capabilities, high power density, and long cycle life[4-10]. They are categorized into electric double-layer capacitors (EDLCs) and pseudocapacitors based on their storage mechanisms[11-13]. In EDLCs, the charging and discharging processes involve the complete adsorption and desorption of charges. The electrode materials used in EDLCs are primarily carbon materials with large surface areas, such as activated carbon (AC), hierarchically porous carbon (HPC), carbon nanotubes (CNT), graphene (GH), *etc.*[14-18]. The pore structures of these materials can be classified as micropores (less than 2 nm), mesopores (2-50 nm), and macropores (greater than 50 nm). Each pore structure offers unique advantages, but also comes with specific performance limitations. The microporous structure provides more active sites, but is not conducive to the transport of electrolytes and active substances. Macropores form the foundation and skeleton of the construction of conductive network and pore structure. They have large pore volume and transport channels, but low specific surface area and insufficient reactive sites. Enhancing EDLC performance relies on designing and creating multi-pore structures to increase the surface area of carbon materials[19-22].

Biomass materials, with advantages such as being environment-friendly, sustainable, rich in heteroatoms, and cost-effective, have become the preferred choice for preparing EDLC electrode materials in recent years[23-26]. So far, a large amount of plant- or animal-derived biomass materials have been used to produce electrode materials for SCs with excellent electrochemical properties[26-28]. Ghosh *et al.* prepared AC from banana stem, corncob (CC) and potato starch by KOH activation or simple carbonization, in which the specific capacitance of KHC was about 225 F g^{-1} at 5 A g^{-1}. In addition, they assembled KHC as a SC; after 6,000 cycles, the capacitance retention is 72.88%[29]. Lin *et al.* used nitrogen-rich soybean as the precursor to prepare nitrogen-doped graded mesoporous micro carbon (ANPC) by coupling template method and KOH activation. They also studied its SC performance and REDOX ability[30]. Finally, the material prepared by the mass ratio of KOH to carbon of 3:1 exhibits the largest specific surface area and the best performance, with a specific capacitance of 243.2 F g^{-1} at 0.5 A g^{-1}. Furthermore, Jung *et al.* also proposed a method for preparing graded porous biomass-derived GH-based carbons by glucose-based polymers[31]. They first transformed the glucose-based polymer into a three-dimensional (3D) foam-like structure, then carbonized it to form the corresponding structure, and finally activated the carbon by physical and chemical ways to produce micro and mesopores, resulting in layered porous biomass-derived GH-based carbon. The specific

capacitance of this material is 175 F g^{-1} at 1 A g^{-1}, and the assembled SC has a maximum energy density of 74 Wh kg^{-1}, corresponding to a maximum power density of 408 kW kg^{-1}. Despite the advancements in biomass materials for SCs, several challenges remain: (1) Limited specific surface area. For example, plant-derived biomass has an abundance of macroporous and mesoporous structures due to the presence of lignin and cellulose, but it rarely contains microporous structures, making it difficult for the material to provide more active sites; (2) Complex preparation process. Biomass, as a natural carbon source, contains a deficiency of heteroatoms in its original composition, which is typically used as a hard template to form hierarchical porous carbon structures through a complex heteroatom doping process; and (3) Uneven pore size distribution. Biomass, when used as a carbon-based material obtained through traditional carbonization, hydrothermal, or activation procedures, presents challenges in precisely regulating the pore size distribution on its surface. To further address these issues, we are using biomass and industrial wastes containing inorganics of various sizes as raw materials, providing a new perspective for the preparation of electrode materials for SCs with high surface area, reasonable porosity, and high performance.

CC, a lignocellulosic byproduct of corn threshing and refinement, is rich in cellulose, hemicellulose, and lignin, endowing it with desirable mechanical properties such as superior tensile strength, enhanced hygroscopicity, and exceptional abrasion resistance. As a biomass residue, CC has found applications across various industries, including abrasive polishing, desiccant materials, and nutritional feed additives, which positions it as a promising precursor for the large-scale synthesis of carbonaceous substrates[32]. Moreover, the intrinsic carbohydrate and crude protein content within CC offers the potential for *in situ* heteroatom doping, specifically nitrogen and oxygen, within the carbon matrix. Fly ash (FA), a particulate byproduct of fossil fuel combustion, is composed primarily of inorganic oxides such as SiO_2, Al_2O_3, Fe_2O_3, and CaO, along with a residual carbon content[33,34]. The fine particle size and smooth surface texture of FA necessitate its responsible management to prevent environmental contamination. Although FA has been repurposed in various applications, ranging from cementitious materials to agronomic fertilizers, as well as in wastewater treatment and industrial recycling, its potential in the synthesis of electrode materials for energy storage devices such as SCs is a rapidly emerging field of interest[35].

In light of the above considerations and with a commitment to eco-friendly materials science, we have crafted an advanced strategy for the two-step hybrid conversion of materials. This process involves hydrothermal carbonization followed by activation to fabricate N/O co-doped, porous biomass-derived carbon. The hydrothermal carbonization phase promotes the selective decomposition of lignin and hemicellulose, thereby enhancing the mesoporosity and oxygenation of the carbon framework, which are crucial for improving electrochemical performance, particularly specific capacitance. This innovative strategy not only leverages the synergistic integration of these two waste streams but also introduces a groundbreaking method for fabricating advanced electrode materials for energy storage applications, highlighting the potential for valorizing industrial byproducts. The porous carbons derived from CC and FA, designated as CFCs, boast a 3D macroporous framework combined with microporous and mesoporous structures. They exhibit a high specific surface area of 1,768 m^2 g^{-1}, which marks an enhancement factor exceeding 70, thereby significantly amplifying the void fraction of the material. The specific capacitance of the sample in 6 M KOH electrolyte, measured using a three-electrode system, was as high as 240 F g^{-1} (at 1 A g^{-1}). In addition, we found that the material has surprising lithium storage properties, with an initial energy density of 160 mAh g^{-1} (at 0.1 A g^{-1}). After 100 cycles, the specific capacity remains at 50 mAh g^{-1}, with a coulomb efficiency of nearly 100%. The successful preparation of this material provides a new idea for energy recycling.

EXPERIMENTAL

Material

The CC with a size of about 20 mesh is purchased from a food processing plant in Jiangsu province, China. FA with a size of about 300 mesh is purchased from an environmental protection company Henan province, China. Highly conductive graphene (HCG) and single-wall CNTs (SWNs) are purchased from Angxing New Carbon Materials Changzhou Co., Ltd., China. Polyvinyl pyrrolidone (The average molecular weight is 58000, K30 PVP), acetonitrile (ACS, ≥ 99.5% CH_3CN), hydrochloric acid (AR, 36%-38% HCl), ethyl alcohol (AR, 99.7% C_2H_5OH), and potassium hydroxide (AR, 90% KOH) are purchased from Sinopharm Chem. Reagent Co., Ltd., China.

Preparation of porous carbons

CC and FA are mixed in a 1:2 ratio and then ball-milled for 12 h to get a fine mixture. A portion of 3 g of this mixture is dispersed in 20 mL 3 M HCl and then transferred to the inner tank of the hydrothermal kettle. After sealing the hydrothermal kettle, it is placed in an oven, and the temperature is raised to 200 °C for 2 h. The hydrothermal product is washed with deionized water until neutral, filtrated, and dried. The product is then soaked in 10 mL 6 M KOH for 12 h and subsequently transferred to an oven at 80 °C to evaporate any remaining liquid. Finally, the mixture is placed in a tube furnace protected by nitrogen atmosphere for carbonization. The temperature is increased to 700 °C at a rate of 2 °C s^{-1} and held for 3 h. After the furnace cools to room temperature, the sample is taken out, washed with 1 M HCl and dried in an oven at 80 °C overnight. The resulting product is named CFC; in addition, samples containing only CC or FA are prepared using the same method, named CC and FAC, respectively.

Preparation of self-supporting electrodes

Due to the complex preparation process of the electrode and the tendency for active material to detach from the substrate during long-term immersion in the electrolyte in a three-electrode test, we propose a method to fabricate self-supporting electrodes: CFCs, HCG, SWNs and PVP are added to acetonitrile with a ratio of 5:4:1:2, stirred for 2 h and then dispersed evenly with an ultrasonic cell crusher. The mixture is then filtered to form a film. This self-supporting has good conductivity, strength and toughness, making it suitable for a variety of test systems.

Characterization

This study uses Scanning Electron Microscopy (SEM, Hitachi S-4800) and Transmission Electron Microscopy (TEM, Fei Tecnai G2 F30) for the microstructural characterization of the sample materials. Chemical state and elemental composition analysis of the samples is conducted using X-ray Photoelectron Spectroscopy (XPS) on an Axis Ultra DLD (Kratos) spectrometer equipped with a monochromatic Al-Kα X-ray source. X-ray Fluorescence (XRF, Axios wavelength dispersive XRF spectrometer) is utilized to analyze the composition of FA qualitatively and quantitatively. The specific surface area and pore size distribution of the samples are measured using a nitrogen adsorption and desorption apparatus (Micromeritics ASAP 2020, USA) and are calculated according to the Brunauer-Emmett-Teller (BET) theory. Additionally, the mesopore volume and radius are determined using the Berret-Joyner-Halenda (BJH) method.

Electrochemical measurements

The electrochemical properties of the samples are evaluated using the CHI660D electrochemical workstation (Shanghaichenhua, China). Techniques including Cyclic Voltammetry (CV), Chronopotentiometry (CP), Electrochemical Impedance Spectroscopy (EIS), and cycle stability tests are performed within a conventional three-electrode configuration, utilizing a 50 mL 6 M KOH electrolyte solution. The working electrode consists of the prepared self-supporting electrodes; the counter electrode is

a platinum (Pt) foil (2 × 2 cm^2), and the reference electrode is a Hg/Hg_2O electrode. CV measurements are conducted within a voltage range of -1.3 to 0.6 V, with scan rates varying from 0.01 to 1 V s^{-1}. CP measurements are taken with a charge and discharge voltage range of -1.2 to 0.4 V, and current densities range from 1 to 8 A g^{-1}. EIS measurements are carried out over a frequency range of 0.1 to 10^5 Hz, with a 5 mV voltage amplitude.

The gravimetric specific capacitance (C_s, F g^{-1}) of the prepared samples is computed from the discharge curve in accordance with[36-38]:

$$C_S = \frac{C}{m} = \frac{I \times t}{\Delta V \times m} \tag{1}$$

Herein, I represents the current (A), t is the discharge time (s), ΔV is the discharge voltage range (V), and m is the mass of the active material on the working electrodes (g).

The energy density (E_d) and the power density (P_d) of SC electrodes can be respectively calculated based on [39-41]:

$$E_d(Wh\ kg^{-1}) = \left(\frac{I}{m}\right)\frac{\int V(t)dt}{3.6} \tag{2}$$

$$P_d(W\ kg^{-1}) = \frac{3.6E_d}{\Delta t} \tag{3}$$

where I is the current (A), m is the mass of the active material on the working electrodes (kg), $\int V(t)dt$ is the integral of the discharge curve, and Δt is the discharge time (h).

Preparation of lithium-ion battery

In this research, the CR2032 button battery case is employed to assemble the lithium-ion battery, with the process accomplished in an atmosphere-protected glove box. First of all, place the prepared self-supporting electrode on the positive electrode shell, and then put the polypropylene (PP) diaphragm and drop the appropriate electrolyte on it to moisten it. Next, position the lithium sheet at the center of the PP diaphragm, then place the nickel foam on the lithium sheet and drop the appropriate electrolyte, and subsequently cover the negative shell. Finally, the device is encapsulated under pressure. The EIS and CV of the battery are tested by Zhner Electrochemical Workstation (Hong Kong Global, China), and in addition, the charge and discharge, rate performance and cycle performance are tested by the Xinwell TC53 battery test system.

RESULTS AND DISCUSSION

Figure 1 shows a schematic diagram depicting the preparation of CFC. Low-cost CC and industrial waste FA are used as a self-template and template, respectively. The precursors are obtained by hydrothermal reaction to remove the existing metal oxides and retain the microporous structure. Then, the microporous and mesoporous structures are realized by high temperature carbonization and activation of KOH under N_2 atmosphere.

Figure 2 shows the surface morphology of CC and FA before and after treatment respectively. As depicted in Figure 2A, untreated CC exhibits a substantial volume characterized by numerous large pores on its surface, approximately 25 μm in diameter. As can be further observed from the illustration, its surface is smooth with almost no pore structure. After being treated with hydrothermal and KOH activation

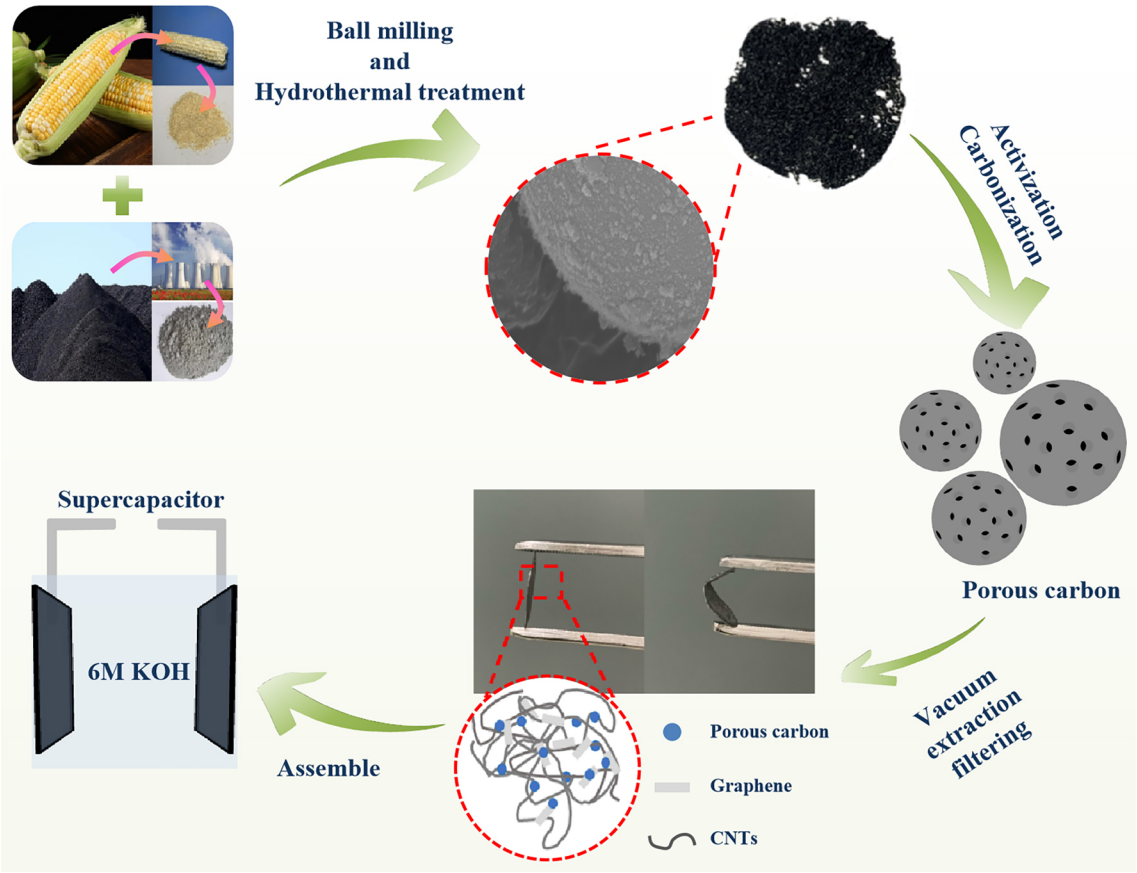

Figure 1. A schematic illustration of CFC preparation by CC and FA.

[Figure 2B], the original pores on the CC surface disappear and are replaced by large pores. Through careful observation, it can be found that the size of these pores is similar to that of the original pores. It acts as a support and frame for the material. In addition, it can also be observed from the illustration that the surface of the CC at this time is still smooth, and there is only a large hole structure. Figure 2C shows FA without any treatment where it is clearly observed to consist of many balls and lumps of varying sizes. In order to explore its main components, the material content of FA is analyzed with the help of XRF technology [Supplementary Tables 1 and 2]. It can be inferred that in addition to unburned carbon, it also mainly contains silicon oxide, calcium oxide, iron oxide, alumina and some trace metal oxides. During the reaction process, these metal oxides become embedded in the CC surface and are subsequently removed through treatment to facilitate initial pore formation. As illustrated in Figure 2D, a limited number of mesopores and larger pores emerge on the surface of FA following hydrothermal and KOH activation treatments, with pore sizes ranging from 10 to 500 nm. This observation suggests that unburned carbon within FA can also interact with metal oxides to generate pore structures. However, given the restricted availability of carbon sources in FA, the energy conversion efficiency remains minimal.

Figure 3A and B illustrates the morphology of carbon foam composites (CFC) synthesized from the two materials which reveals two distinct morphologies: block and spherical forms within the CFC structure. Furthermore, they demonstrate that both morphological contain macroporous and mesoporous structures with pore sizes ranging from 10 to 500 nm, indicating a significant increase in pore quantity compared to treatments involving FA alone. The emergence and proliferation of these pores suggest that porous carbon

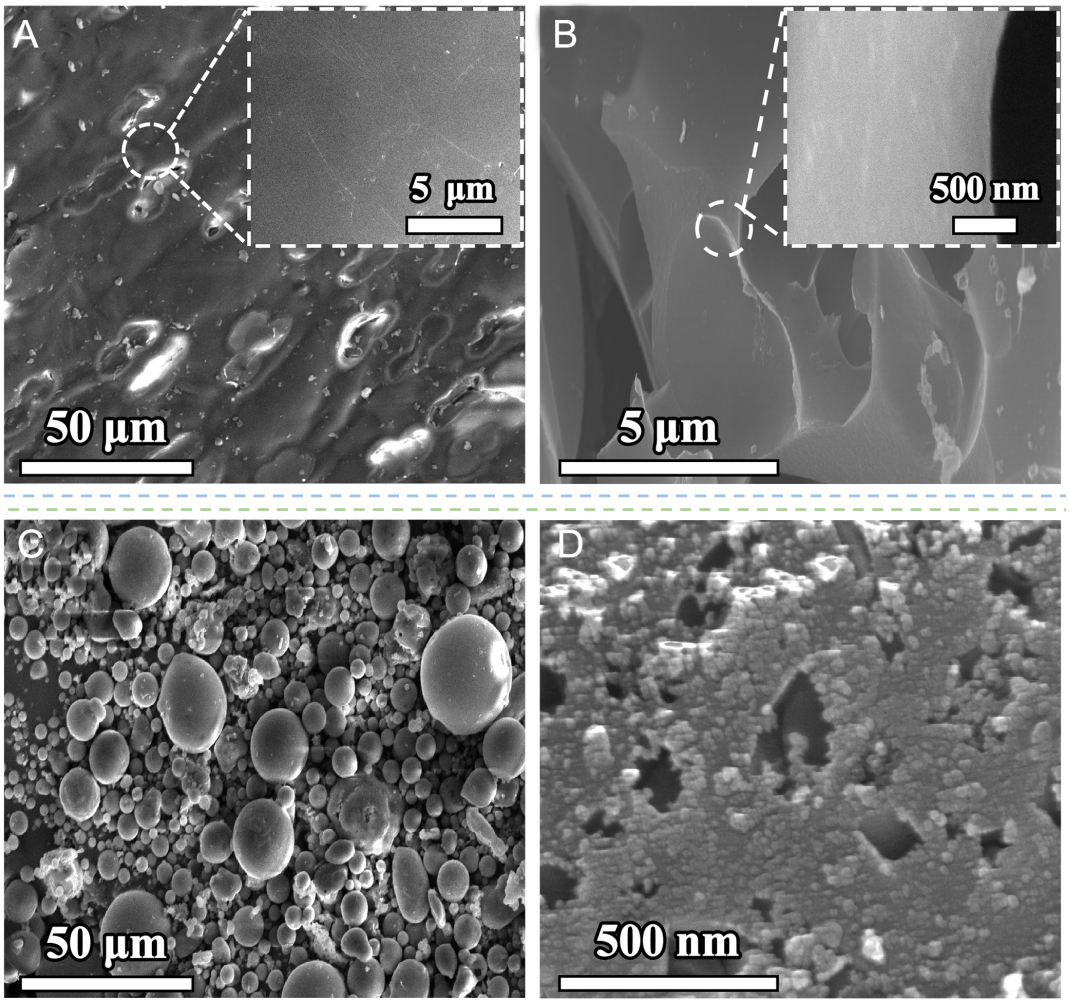

Figure 2. SEM images of (A and B) Before and after processing of CC; (C and D) Before and after processing of FA.

is successfully synthesized through the synergistic interaction between CC and FA, resulting in a novel morphology characterized by porous carbon microspheres.

To investigate the co-pore formation mechanism between CC and FA and the origin of porous carbon microspheres, we delve into an extensive examination of their preparation process. Supplementary Figure 1 presents the micro-morphology of CC, FA, and CFC precursors following hydrothermal treatment. As observed in Supplementary Figure 1A, numerous carbon microspheres are generated on the surface of CC after water heating. These microspheres exhibit smooth surfaces but display uneven diameters; some appear to be dissolving. Consequently, it can be inferred that these carbon microspheres may gradually detach from larger blocks or spheres over time. Subsequently, controlling hydrothermal duration allows for regulation of the size of these carbon microspheres. Supplementary Figure 1B and C presents scanning electron microscopy images of FA following hydrothermal treatment at varying magnifications. It is evident that the aforementioned phenomenon does not manifest in FA post-hydrothermal reaction; however, under high magnification, irregularly sized pores are observable on the material's surface. This observation supports the hypothesis that metal oxides within FA interact with unburned carbon during hydrothermal processing to create these voids. In contrast, the morphology of the CFC precursor exhibits slight differences compared to the two previously discussed materials [Supplementary Figure 1D and E]. Notably, this material displays

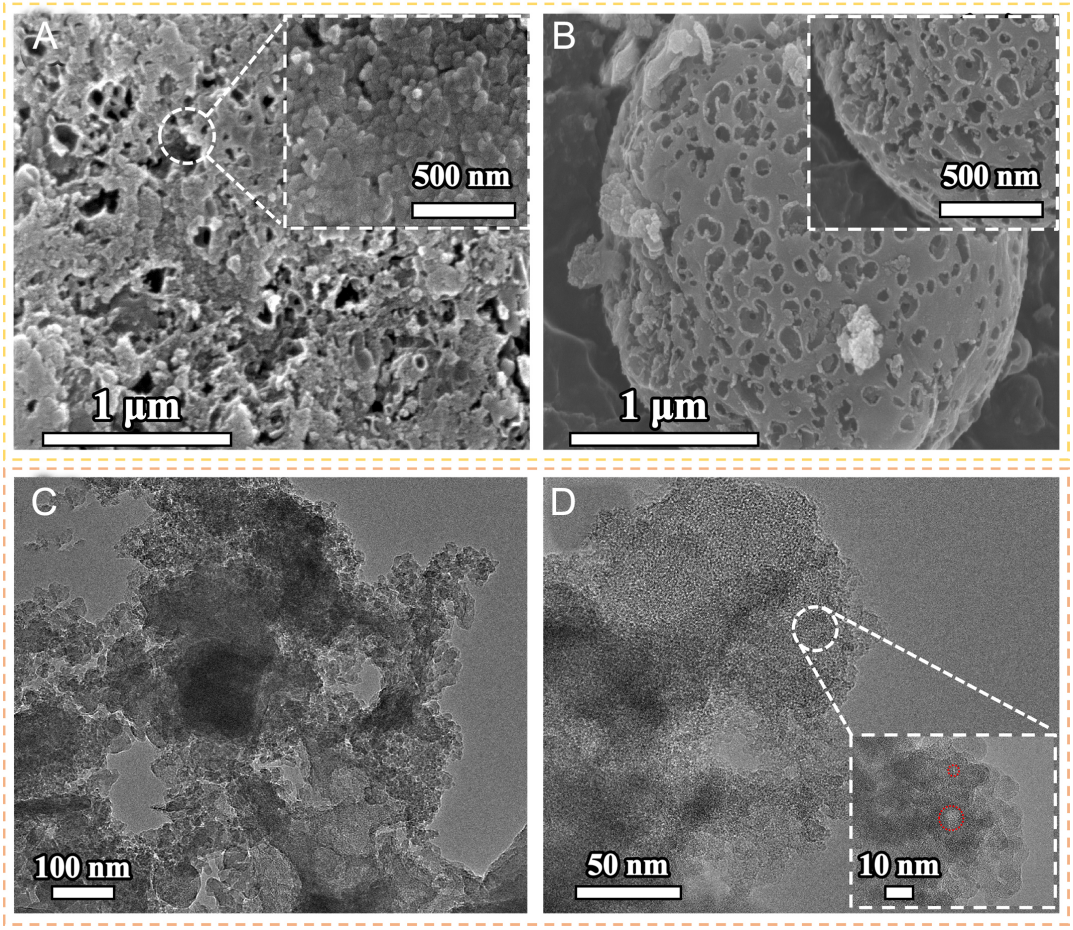

Figure 3. (A and B) SEM images of CFC at different magnifications; (C and D) TEM images of CFC.

both block structures and carbon spheres derived from those blocks simultaneously. As illustrated in Supplementary Figure 1D, the surface of carbon microspheres in this sample is not smooth but rather features numerous fine particles. Based on prior analyses regarding CC hydrothermal behavior, it can be inferred that these carbon microspheres primarily originate from direct fragmentation of larger blocks or by division of individual microspheres into smaller ones; thus, it is reasonable to conclude that these minute particles result from contributions made by FA. Furthermore, high-magnification images [Supplementary Figure 1E] reveal a limited presence of carbon microspheres on the surface of corn pellets while indicating significant preliminary pore formation effects as well. Overall, the porous structure development within CFC predominantly arises from metal oxide intercalation found in FA; concurrently, some remain adhered to the carbon surfaces as fine particles. Following activation and high-temperature carbonization processes, these particles may either be removed or etched away to yield porous characteristics on the underlying carbon substrate. Additionally, CC - serving as biomass-derived carbon - produces a substantial quantity of carbon microspheres during hydrothermal treatment which enriches material architecture and provides critical value for subsequent strategies aimed at preparing porous carbon microsphere structures.

Figure 3C and D shows TEM images of CFC. It can be clearly seen that the material is amorphous carbon and has mesoporous structure with a diameter of about 10-50 nm. From the marked area and the inset part,

it can be observed that there are some bright spots of light transmission on the material, which we speculate may be microporous structures. The existence of these microporous structures may be attributed to two factors: on the one hand, the rich element composition inside the CC will react into gas and escape at high temperatures, and on the other hand, CC, as a plant, originally has many micropores. In summary, we successfully prepared CFC porous biomass carbon with abundant macroporous, mesoporous and microporous structures through the synergistic effect of CC and FA. The existence of these pores plays a positive role in electrolyte transport and the active site of electrochemical reaction, which can effectively improve the electrochemical performance of electrode materials.

The elemental composition and chemical bonds of the CFC are further analyzed through the XPS spectra presented in Figure 4. First, the C 1s peak of CFC can be divided into five main components, C=C (284.3 eV), C-C (284.9 eV), C-N (286.6 eV) and C-O/C=N (288.2 eV), and the peak at 294.6 eV is characterized by π-π oscillation[42-44]. As can be seen from Figure 4B, the N 1s XPS spectrum of CFC consists of four peaks - quinoid amine (=N-, 398.6 eV), pyrrole -N (399.6 eV), benzene (-NH-, 400.5 eV), and nitrogen cation radical (N^+,401.8 eV) - with azane type (402.3 eV) at the center[23,45,46]. The presence of the azane type indicates a cross-linking structure. The combination of nitrogen functionalities such as pyrrole, pyridine, and graphitic nitrogen boosts the pseudocapacitance characteristics of the electrode, thus enhancing its energy storage capability. Moreover, nitrogen doping improves the wettability of the electrode material, facilitating a more efficient interaction with electrolyte ions. This outstanding interface lowers the equivalent series resistance (ESR), promotes charge transfer kinetics, and eventually raises the power density and accelerates the charge and discharge kinetics. Additionally, nitrogen doping is capable of enhancing the conductivity of the carbon substrate. The insertion of nitrogen atoms disrupts the sp^2 carbon matrix, generating additional defects that make electron transfer more effortless. This increase in conductivity leads to an enhanced rate capability and overall superior performance of SCs[36,37]. Finally, the O 1s peak, as seen in Figure 4C, can be deconvoluted into three characteristic peaks: C=O (531.4 eV), C-O (532.4 eV) and -COOH (533.2 eV), respectively[47-49]. The existence of oxygen-containing groups can enhance the hydrophilicity, allowing the ions in the water system electrolyte to permeate the material more easily. The Raman spectra for CC, FA, and CFC are depicted in the Supplementary Figure 2. Their I(D)/I(G) ratios are 1.03, 1.01, and 0.99, respectively, indicating that CFC exhibits a greater degree of graphitization. A sharp peak at 2,949 cm^{-1} is observed in all three materials, signifying the stretching vibration of the O-H bond. Notably, FA possesses a distinctive 2D peak characteristic of GH at 2,549 cm^{-1}.

In order to investigate the specific surface area and pore size distribution of the material, nitrogen adsorption/desorption test was carried out. First of all, it can be seen from the above SEM photos that the surfaces of CC and FA before treatment are smooth, and the existence of holes is almost invisible. Since their nitrogen absorption and desorption curves are irregular and do not close, and their specific surface areas are less than 1 $m^2 g^{-1}$, the test results will not be shown or detailed. Supplementary Figure 3 shows the nitrogen absorption and desorption of the three materials after hydrothermal treatment. It can be seen that the absorption and desorption curves of the three materials are all type IV isotherms[50,51]. The failure of the absorption and desorption curves of the CC in Supplementary Figure 3A may be caused by the small specific surface area of the material itself and the insufficient amount of test samples. There is no obvious rapid rise of adsorption lines in the low-pressure region, indicating almost no microporous structure in the three curves. Platforms and hysteresis loops appear in the middle pressure region and the high-pressure region, indicating that they have mesoporous and macroporous structures. In addition, their specific surface area is slightly increased compared with that before treatment, while the specific surface area of FA and mixture is larger, indicating that the addition of FA plays a positive role in the formation of pores, and the preliminary pore-making begins to take effect.

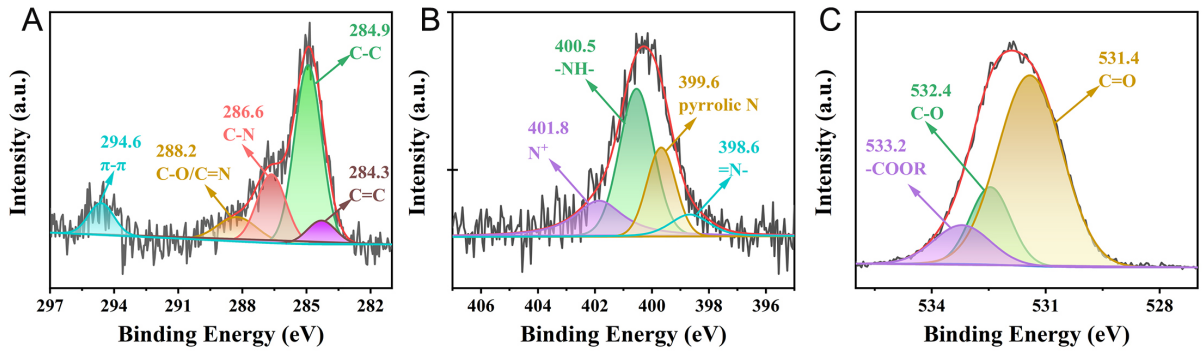

Figure 4. XPS deconvoluted spectrum of (A) C 1s, (B) N 1s and (C) O 1s of CFC.

The sample adsorption and desorption curves after activation and carbonization are shown in Figure 5. It can be seen from Figure 5A that the adsorption-desorption isotherm of CC after complete porosity is a type I isotherm[52,53], and there is a steep long platform in this curve, reflecting the reversible adsorption process of a single layer, indicating that the material has a microporous structure. Therefore, it can be concluded that the simple CC porosity can only have a microporous structure, but cannot achieve multi-layer porous carbon structure.

Figure 5C shows that the adsorption-desorption isotherm of CFC exhibits a type IV mesoporous characteristic curve; when $P/P_0 < 0.01$, the adsorption line obviously rises rapidly, indicating the existence of micropores in CFC. Further adsorption of N_2 reveals a plateau in the adsorption curve where P/P_0 is between 0.2-0.5. With the increase of P/P_0 from 0.5 to 0.9, the adsorption line gradually rises, forming a H2 hysteresis loop related to capillary condensation, which manifests the characteristics of mesoporous surface. In the range of P/P_0 = 0.9-1.0, the adsorption line continues to rise, and does not show an obvious adsorption plateau as it approaches 1.0, exhibiting an H3 hysteresis loop, which indicates the existence of macropore distribution. In addition, the pore size distribution diagram in the illustration shows that the pore size of CFC is mostly concentrated in the ranges of 1.5-1.3, 3.5-4 and 10-15 nm, indicating a combination of microporous, mesoporous and mesoporous structures[54,55].

The same phenomenon can be found in the nitrogen adsorption/desorption curve of FAC [Figure 5B], but the sample has a small distribution of large pores, with a specific surface area of only one-third that of CFC, possibly due to insufficient carbon sources in FA. The above results show that the core-making of FA and CC can greatly increase the specific surface area of carbon materials. On the one hand, CC, as a biomass material, provides a large number of microporous and macroporous channels and a stable carbon source. On the other hand, the macromolecules and unburned carbon in FA itself can be used as templates and self-templates to generate mesoporous structures.

In Figure 6A, the CV plot of the CFC measured by 6 M KOH electrolyte in the three-electrode system is plotted. At negative potential (-0.6-0 V), the curve appears a plateau, indicating that the electrochemical reaction of the CFC at low potential is dominated by charge absorption and desorption, which shows a double-layer capacitance behavior. It can complete the transmission and diffusion of electrons and ions within a short time, manifesting that it has good capacitance characteristics. As the potential increases, the curve reveals the emergence of REDOX peaks within the range of 0.6-1.3 V, indicative of pseudocapacitive behavior. These peaks are attributed to the reversible REDOX reactions of the functional groups doped with heteroatoms during the charge and discharge processes. The XPS spectrum reveals the presence of various nitrogen-containing functional groups within the CFC, including quinoid amine, pyrrole-N, benzene-NH-,

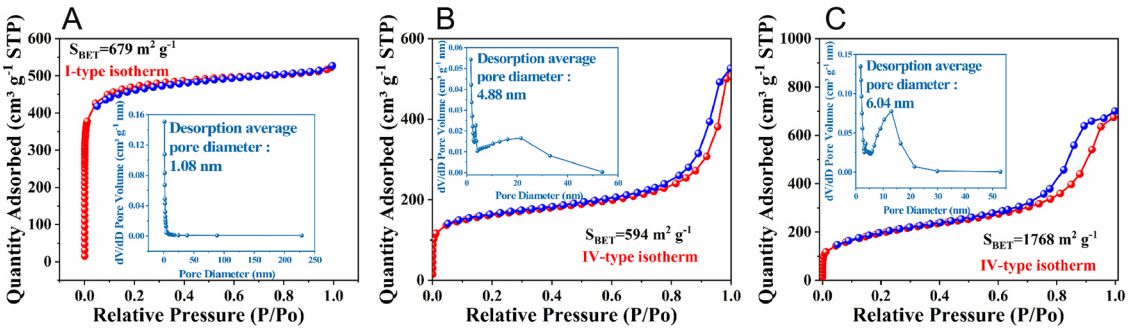

Figure 5. (A-C) Nitrogen adsorption/desorption isotherms and pore size distribution diagram of CC, FAC, and CFC.

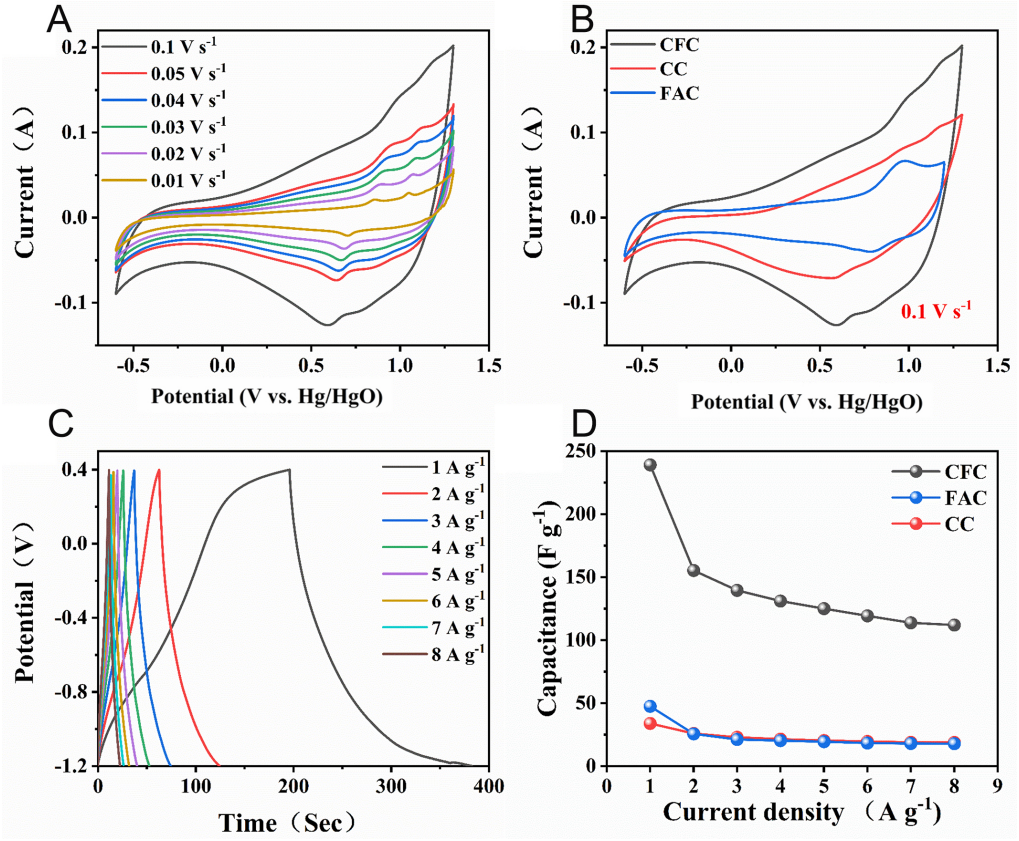

Figure 6. (A) CV curves at different scanning speeds of CFC, (B) CV curve of CFC, CC and FAC with a scanning speed of 0.1 V s^{-1}, (C) the constant current charge and discharge curve at different current densities of CFC, and (D) the specific capacitance of CFC, CC and FAC.

and nitrogen cation radicals. The integration of these functional groups contributes to the enhancement of the electrode's pseudocapacitive characteristics, thereby augmenting its energy storage capacity. At different scanning speeds (1-8 A g^{-1}), the shape of each curve is similar, the response current increases with the rise of scanning speed, and the REDOX peak position rarely has displacement, which indicates that the electrode material has good cycle reversible stability and fast REDOX current response. This phenomenon can also be easily seen from the CV curves of CC and FAC materials in Supplementary Figure 4A and B. It can be found from Figure 6B that the CV area and response current of CFC prepared by CC and FA are larger than

Table 1. Electrochemical performances of different precursor electrodes

Precursor	Electrolyte	Current density	SSA	Specific capacitance	Ref.
Reed straw	6 M KOH	1 A g^{-1}	547.1 m^2 g^{-1}	202.8 F g^{-1}	[56]
Peanut shell	6 M KOH	1 A g^{-1}	2,764 m^2 g^{-1}	228 F g^{-1}	[57]
Biomass fulvic acid	TEABF4/PC	1 A g^{-1}	1,938 m^2 g^{-1}	107 F g^{-1}	[58]
Fatsia japonica	6 M KOH	1 A g^{-1}	870.3 m^2 g^{-1}	140 F g^{-1}	[59]
Ambrosia melon peels	1 M H_2SO_4	1 A g^{-1}	529.9 m^2 g^{-1}	200 F g^{-1}	[60]
Passion fruit husks	1 M trifluoroacetic acid	1 A g^{-1}	1,858 m^2 g^{-1}	297.1 F·g^{-1}	[61]
Camellia	1 M KOH	2 A·g^{-1}	/	125.42 F·g^{-1}	[62]
Corncob and fly ash	6 M KOH	1 A g^{-1}	1,768 m^2 g^{-1}	240 F g^{-1}	This work

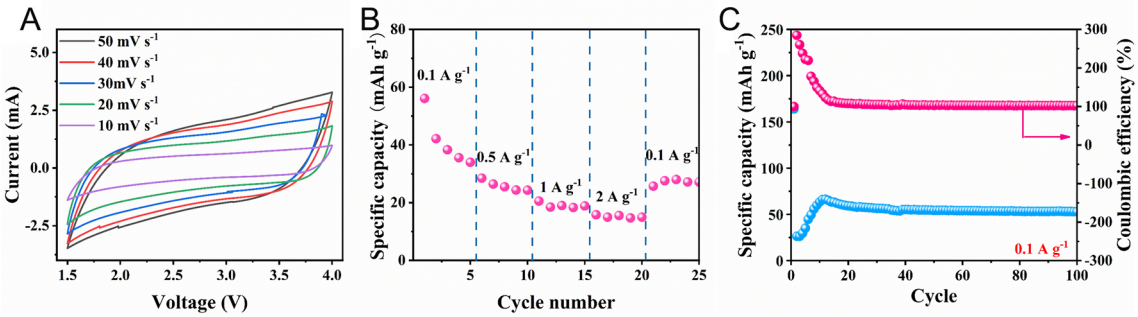

Figure 7. (A) CV curves at different scanning speeds of CFC half-cell, (B) magnification performance of CFC half-cell, (C) cycle performance of CFC half-cell.

those of the other two materials prepared by monomers; meanwhile, a pair of REDOX peaks possessed by CC (at 0.6 and 1.1 V approximately) and FAC (at 0.8 and 0.9 V approximately) are reflected in CFC respectively. It is worth noting that we can also observe that the potential range of CFC is -0.6-1.3 V, and the potential difference reaches 1.9 V, which is relatively scarce in aqueous electrolytes. Figure 6C, Supplementary Figure 4C and D illustrate that the charge-discharge profiles of the various samples at distinct current densities (1-8 A g^{-1}) exhibit favorable rate capabilities. Notably, CFC demonstrates the longest discharge duration at a current density of 1 A g^{-1}. Figure 6D visually depicts that the specific capacitance of CFC is markedly superior to that of CC and FAC across different current densities, with CFC achieving a specific capacitance of 240 F g^{-1} at 1 A g^{-1}. This suggests that the CFC, prepared through the collaborative efforts of CC and FA, possesses a greater specific surface area and a higher number of functional groups, enabling a greater number of active sites to be utilized on the surface of the CFC. Nevertheless, the specific capacitance of the CFC diminishes progressively as the current density increases, which we attribute to the possibility that the REDOX reactions and charge transfer rates of the active material may not suffice to accommodate the abrupt rise in current. The collective results of these tests underscore the outstanding performance of CFC, which also compares favorably with several previously reported materials in the literature [Table 1].

Except for the research on the electrical properties for SC of CFC, we also assemble a half-cell using the lithium sheet as the counter electrode to test its lithium storage performance in a lithium electrolyte. Figure 7A is the CV map of CFC measured at different sweep speeds under the voltage window of 1.5-4 V. All curves are roughly symmetrical and rectangular, which is a typical double-layer capacitance characteristic, indicating that the main occurrence of the material is the adsorption and desorption of lithium ions on the material surface. The rate characteristics of CFC are recorded in Figure 7B. When the current density increases to 2 A g^{-1}, the capacity is maintained at 53.2%. After switching back to 0.1 A g^{-1}, the

reversible capacity is maintained at 67.7%, showing good rate performance. Figure 7C shows the cycle performance of the half-cell at 0.1 A g^{-1}. The initial capacity is about 160 mAh g^{-1}. Although there is significant attenuation in the first 10 cycles, the capacity gradually rises and basically remains stable thereafter. After 100 charging and discharging cycles, the specific capacity stabilizes at 50 mAh g^{-1}, demonstrating excellent cycle stability. The aforementioned results suggest that the materials also possess lithium storage properties, but the lithium storage mechanism and performance enhancement still require further investigation.

CONCLUSIONS

In this study, biomass carbon (CC) and industrial waste (FA) are successfully employed together for the preparation of CFC through the hydrothermal method and KOH activation, thereby achieving waste recycling. The results showed that the participation of FA effectively increased the mesoporous ratio of the material and thus enriched the specific surface area of the material. Simultaneously, a considerable number of carbon microspheres generated in the hydrothermal process of biomass CC enriched the microstructure of the electrode material and increased the heteroatom doping site. In the three-electrode test, CFC shows a maximum specific capacitance of 240 F g^{-1} (at 1 A g^{-1}), and even at 8 A g^{-1}, the specific capacitance can reach over 100 F g^{-1}, with good reversibility and magnification performance. In addition, CFC also displays excellent lithium storage capacity. When the current density is 0.1 A g^{-1}, the first discharge specific capacity of the assembled Li|CFC capacitor is about 160 mAh g^{-1}, and the specific capacity can be maintained at 50 mAh g^{-1} after 100 cycles. This strategy leverages the synergistic action between different materials to prepare porous carbon, offering a new idea for increasing the specific surface area of materials and comprehensively improving electrochemical properties.

DECLARATIONS

Authors' contributions

Conceived the ideas of the work and carried out the basic characterization, including TEM and SEM measurement, prepared the devices and performed most measurements, including CV, GCD, and cyclic stability: Ruan, S.

Helped to conduct the measurements and analysis: Huang, H.; Gan, Y.

Involved in the data analysis and wrote the final version of the manuscript: Ruan, S.; He, X.; Xia, Y.

Supervised this project: Zhang, J.; Zhang, W.; Xia, X.

Analyzed the data and contributed to the discussions: Ruan, S.; He, X.; Huang, H.; Gan, Y.; Xia, Y.; Zhang, J.; Wan, W.; Wang, C.; Xia, X.; Zhang, W.

Availability of data and materials

The rata data supporting the findings of this study are available within this Article and its Supplementary Material. Further data are available from the corresponding authors upon request.

Financial support and sponsorship

This work is supported by Department of Science and Technology of Zhejiang Province (Grant No. 2023C01231), Key Scientific Research Project of Hangzhou (Grant No. 2024SZD1B12), National Natural Science Foundation of China (Grant Nos. 52372235, 52073252, KYY-ZX-2020050), Postdoctoral Research Project of Zhejiang Province (ZJ2024101), and Key Laboratory of Engineering Dielectrics and Its Application (Harbin University of Science and Technology), Ministry of Education (KFM 202302).

Conflicts of interest

All authors declared that there are no conflicts of interest.

Ethical approval and consent to participate

Not applicable.

Consent for publication

Not applicable.

REFERENCES

1. Yu, F.; Li, S.; Chen, W.; Wu, T.; Peng, C. Biomass-derived materials for electrochemical energy storage and conversion: overview and perspectives. *Energy. Environ. Mater.* **2019**, *2*, 55-67. DOI
2. Yang, C.; Wu, H.; Cai, M.; et al. Valorization of biomass-derived polymers to functional biochar materials for supercapacitor applications via pyrolysis: advances and perspectives. *Polymers* **2023**, *15*, 2741. DOI PubMed PMC
3. Khedulkar, A. P.; Pandit, B.; Dang, V. D.; Doong, R. A. Agricultural waste to real worth biochar as a sustainable material for supercapacitor. *Sci. Total. Environ.* **2023**, *869*, 161441. DOI PubMed
4. Srikanth, V. V.; Ramana, G. V.; Kumar, P. S. Perspectives on state-of-the-art carbon nanotube/polyaniline and graphene/polyaniline composites for hybrid supercapacitor electrodes. *J. Nanosci. Nanotechnol.* **2016**, *16*, 2418-24. DOI PubMed
5. Hao, H.; Tan, R.; Ye, C.; Low, C. T. J. Carbon-coated current collectors in lithium-ion batteries and supercapacitors: materials, manufacture and applications. *Carbon. Energy.* **2024**, *6*, e604. DOI
6. Zhang, J.; Liu, W.; Du, M.; et al. Kinetic investigation of the energy storage process in graphene fiber supercapacitors: unraveling mechanisms, fabrications, property manipulation, and wearable applications. *Carbon. Energy.* **2025**, *7*, e625. DOI
7. Zhou, J.; Zhu, Z.; Shi, W.; et al. Design strategies and recent advancements of solid-state supercapacitor operating in wide temperature range. *Carbon. Energy.* **2024**, *6*, e504. DOI
8. Das, S. K.; Pradhan, L.; Jena, B. K.; Basu, S. Polymer derived honeycomb-like carbon nanostructures for high capacitive supercapacitor application. *Carbon* **2023**, *201*, 49-59. DOI
9. Fan, Z. S.; Valentino, K. Y.; Chowdhury, S.; et al. Weak base-modulated synthesis of bundle-like carbon superstructures from metal-organic framework for high-performance supercapacitors. *Chem. Eng. J.* **2023**, *462*, 142094. DOI
10. Narayanamoorthi, E.; Gowthaman, N. S. K.; John, S. A.; Elango, K. P. Heteroatom-doped mesoporous carbon derived from covalent organic framework for the potential application of symmetric supercapacitor device. *J. Mol. Struct.* **2024**, *1295*, 136659. DOI
11. Xu, Y.; Yang, X.; Li, X.; Gao, Y.; Wang, L.; Lü, W. Flexible zinc-ion hybrid supercapacitor based on Co^{2+}-doped polyaniline/V_2O_5 electrode. *J. Power. Sources.* **2024**, *623*, 235399. DOI
12. Shaikh, N. S.; Kanjanaboos, P.; Lokhande, V. C.; Praserthdam, S.; Lokhande, C. D.; Shaikh, J. S. Engineering of battery type electrodes for high performance lithium ion hybrid supercapacitors. *ChemElectroChem* **2021**, *8*, 4686-724. DOI
13. Jiang, H.; Liu, J.; Tang, B.; et al. Regulation mechanism on A bilayer Li_2O-rich interface between lithium metal and garnet-type solid electrolytes. *Adv. Funct. Mater.* **2024**, *34*, 2306399. DOI
14. Hasan M, Sayantha Aniv S, Mominul Islam M. Carbon nanosheets-based supercapacitor materials: recent advances and prospects. *Chem. Rec.* **2024**, *24*, e202300153. DOI PubMed
15. Kumar, S.; Saeed, G.; Zhu, L.; Hui, K. N.; Kim, N. H.; Lee, J. H. 0D to 3D carbon-based networks combined with pseudocapacitive electrode material for high energy density supercapacitor: a review. *Chem. Eng. J.* **2021**, *403*, 126352. DOI
16. Lang, J.; Zhang, X.; Liu, B.; Wang, R.; Chen, J.; Yan, X. The roles of graphene in advanced Li-ion hybrid supercapacitors. *J. Energy. Chem.* **2018**, *27*, 43-56. DOI
17. Pour, G. B.; Ashourifar, H.; Aval, L. F.; Solaymani, S. CNTs-supercapacitors: a review of electrode nanocomposites based on CNTs, graphene, metals, and polymers. *Symmetry* **2023**, *15*, 1179. DOI
18. Li, C.; Zheng, C.; Cao, F.; Zhang, Y.; Xia, X. The development trend of graphene derivatives. *J. Electron. Mater.* **2022**, *51*, 4107-14. DOI
19. Zhang, T.; Li, C.; Wang, F.; et al. Recent advances in carbon anodes for sodium-ion batteries. *Chem. Rec.* **2022**, *22*, e202200083. DOI
20. Shen, S.; Huang, L.; Tong, X.; et al. A powerful one-step puffing carbonization method for construction of versatile carbon composites with high-efficiency energy storage. *Adv. Mater.* **2021**, *33*, e2102796. DOI
21. Shen, S.; Chen, Y.; Zhou, J.; et al. Microbe-mediated biosynthesis of multidimensional carbon-based materials for energy storage applications. *Adv. Energy. Mater.* **2023**, *13*, 2204259. DOI
22. Shen, S.; Chen, Y.; Gu, X.; et al. Juice vesicles bioreactors technology for constructing advanced carbon-based energy storage. *Adv. Mater.* **2024**, *36*, e2400245. DOI
23. Ajin, I.; Chandra, B. A. Effects of potassium-based activating agents on the biochar derived from coconut tree husk for enhancing the surface area and supercapacitor performance. *Energy. Fuels.* **2024**, *38*, 11240-52. DOI
24. Choudhary, N.; Singh, S.; Malik, G.; et al. Chemically tuned cellulose nanocrystals/single wall carbon nanosheet based electrodes for hybrid supercapacitors. *Sustain. Energy. Fuels.* **2024**, *8*, 3595-609. DOI

25. Samage, A.; Halakarni, M.; Yoon, H.; Sanna, K. N. Sustainable conversion of agricultural biomass waste into electrode materials with enhanced energy density for aqueous zinc-ion hybrid capacitors. *Carbon* **2024**, *219*, 118774. DOI
26. Huang, L.; Shen, S.; Zhong, Y.; et al. Multifunctional hyphae carbon powering lithium-sulfur batteries. *Adv. Mater.* **2022**, *34*, e2107415. DOI
27. Qiu, Z.; Cao, F.; Pan, G.; et al. Carbon materials for metal-ion batteries. *ChemPhysMater* **2023**, *2*, 267-81. DOI
28. Huang, L.; Qiu, Z.; Liu, P.; et al. Hyphae-mediated bioassembly of carbon fibers derivatives for advanced battery energy storage. *Carbon. Energy.* **2024**, *6*, e470. DOI
29. Ghosh, S.; Santhosh, R.; Jeniffer, S.; et al. Natural biomass derived hard carbon and activated carbons as electrochemical supercapacitor electrodes. *Sci. Rep.* **2019**, *9*, 16315. DOI PubMed PMC
30. Lin, G.; Ma, R.; Zhou, Y.; Liu, Q.; Dong, X.; Wang, J. KOH activation of biomass-derived nitrogen-doped carbons for supercapacitor and electrocatalytic oxygen reduction. *Electrochim. Acta.* **2018**, *261*, 49-57. DOI
31. Jung, S.; Myung, Y.; Kim, B. N.; Kim, I. G.; You, I. K.; Kim, T. Activated biomass-derived graphene-based carbons for supercapacitors with high energy and power density. *Sci. Rep.* **2018**, *8*, 1915. DOI PubMed PMC
32. Song, Y.; Qu, W.; He, Y.; et al. Synthesis and processing optimization of N-doped hierarchical porous carbon derived from corncob for high performance supercapacitors. *J. Energy. Storage.* **2020**, *32*, 101877. DOI
33. Wang, H.; Wang, M.; Zhang, J.; Wang, N.; Wang, J.; Yang, J. Preparation of fly ash-based cobalt-iron silicate as supercapacitor electrode material. *Chem. Eng. J.* **2022**, *434*, 134661. DOI
34. Mushtaq, F.; Wang, L.; Tu, H.; et al. Status of fly ash-derived sustainable nanomaterials for batteries and supercapacitors. *Sustain. Energy. Fuels.* **2024**, *8*, 2798-823. DOI
35. Du, Z.; Li, L.; Shen, G. Proton-conducting hydrogel electrolytes with tight contact to binder-free MXene electrodes for high-performance thermally chargeable supercapacitor. *Carbon. Energy.* **2024**, *6*, e562. DOI
36. Ruan, S.; Xin, W.; Wang, C.; et al. An approach to enhance carbon/polymer interface compatibility for lithium-ion supercapacitors. *J. Colloid. Interface. Sci.* **2023**, *652*, 1063-73. DOI
37. Ruan, S.; Shi, M.; Huang, H.; et al. An innovative design of integrative polyaniline/carbon foam flexible electrode material with improved electrochemical performance. *Mater. Today. Chem.* **2023**, *29*, 101435. DOI
38. Huang, L.; Guan, T.; Su, H.; et al. Synergistic interfacial bonding in reduced graphene oxide fiber cathodes containing polypyrrole@sulfur nanospheres for flexible energy storage. *Angew. Chem. Int. Ed.* **2022**, *61*, e202212151. DOI
39. Huang, B. L.; Zhang, H.; Qiu, Z.; et al. Hyphae carbon coupled with gel composite assembly for construction of advanced carbon/sulfur cathodes for lithium-sulfur batteries. *Small* **2024**, *20*, e2307579. DOI
40. He, X.; Zhuang, T.; Ruan, S.; et al. An innovative poly(ionic liquid) hydrogel-based anti-freezing electrolyte with high conductivity for supercapacitor. *Chem. Eng. J.* **2023**, *466*, 143209. DOI
41. He, X.; Li, W.; Xia, Y.; et al. Pivotal factors of wood-derived electrode for supercapacitor: Component striping, specific surface area and functional group at surface. *Carbon* **2023**, *210*, 118090. DOI
42. Chen, H.; Ericson, T.; Temperton, R. H.; et al. Investigating surface reactivity of a Ni-rich cathode material toward CO_2, H_2O, and O_2 using ambient pressure X-ray photoelectron spectroscopy. *ACS. Appl. Energy. Mater.* **2023**, *6*, 11458-67. DOI
43. Bagus, P. S.; Nelin, C. J.; Brundle, C. R. Chemical significance of X-ray photoelectron spectroscopy binding energy shifts: a Perspective. *J. Vac. Sci. Technol. A.* **2023**, *41*, 068501. DOI
44. Altendorf, S. G.; Takegami, D.; Meléndez-Sans, A.; et al. Electronic structure of the Fe^{2+} compound $FeWO_4$: a combined experimental and theoretical X-ray photoelectron spectroscopy study. *Phys. Rev. B.* **2023**, *108*, 085119. DOI
45. Gautam, A.; Singh, R. S.; Gautam, P.; Hussain, S. M.; Reddy, V. S. X-ray photoelectron spectroscopy and tunable photoluminescence study of gold nanoparticles embedded in PVA films. *Luminescence* **2024**, *39*, e4607. DOI
46. Aditya, D. S.; Mahadevaprasad, K. N.; Santhosh, K. N.; et al. Sustainable and eco-friendly membranes from sugarcane bagasse: an upcycling approach for wastewater treatment and energy storage. *Chem. Eng. J.* **2024**, *488*, 150910. DOI
47. Kavre Piltaver, I.; Peter, R.; Salamon, K.; Micetic, M.; Petravic, M. In situ X-ray photoelectron spectroscopy study of initial stages of tungsten trioxide reduction by low-energy hydrogen bombardment. *J. Phys. Chem. C.* **2024**, *128*, 5345-54. DOI
48. Nandi, P.; Park, H.; Shin, S.; et al. NiO as hole transporting layer for inverted perovskite solar cells: a study of X-ray photoelectron spectroscopy. *Adv. Mater. Inter.* **2024**, *11*, 2300751. DOI
49. Moeini, B.; Gallagher, N.; Linford, M. R. Surface analysis insight note: multivariate curve resolution of an X-ray photoelectron spectroscopy image. *Surf. Interface. Anal.* **2023**, *55*, 853-8. DOI
50. Zubkov, T.; Smith, R. S.; Engstrom, T. R.; Kay, B. D. Adsorption, desorption, and diffusion of nitrogen in a model nanoporous material. II. Diffusion limited kinetics in amorphous solid water. *J. Chem. Phys.* **2007**, *127*, 184708. DOI
51. Zelenka, T. Adsorption and desorption of nitrogen at 77 K on micro- and meso- porous materials: study of transport kinetics. *Microporous. Mesoporous. Mater.* **2016**, *227*, 202-9. DOI
52. Blacher, S.; Alié, C.; Gommes, C.; Lodewyckx, P.; Pirard, R.; Pirard, J. P. Characterisation of silica low-density xerogels in presence of additives by image analysis and nitrogen adsorption-desorption. *Stud. Surf. Sci. Catal.* **2002**, *144*, 323-30. DOI
53. Baldovino-Medrano, V. G.; Niño-Celis, V.; Isaacs Giraldo, R. Systematic analysis of the nitrogen adsorption-desorption isotherms recorded for a series of materials based on microporous-mesoporous amorphous aluminosilicates using classical methods. *J. Chem. Eng. Data.* **2023**, *68*, 2512-28. DOI
54. Dong, S.; Zhao, D.; Li, L.; Li, X.; Chen, T. Study on pore evolution characteristics of gas adsorption and desorption in coal under the

action of liquid nitrogen. *Geosci. J.* **2023**, *27*, 101-12. DOI

55. Dias, A.; Ciminelli, V. S. T. Analysis of nitrogen adsorption-desorption isotherms for the estimation of pore-network dimensions and structure of ferroelectric powders. *Ferroelectrics* **2000**, *241*, 9-16. DOI
56. Liao, Y.; Shang, Z.; Ju, G.; et al. Biomass derived N-doped porous carbon made from reed straw for an enhanced supercapacitor. *Molecules* **2023**, *28*, 4633. DOI PubMed PMC
57. Hu, Z.; Li, X.; Tu, Z.; et al. "Thermal dissolution carbon enrichment" treatment of biomass wastes: supercapacitor electrode preparation using the residue. *Fuel. Proc. Technol.* **2020**, *205*, 106430. DOI
58. Wang, J.; Zhang, C.; Chen, Z.; et al. An environment-friendly method to prepare fulvic acid-based porous carbon for high energy density supercapacitors. *Diam. Relat. Mater.* **2024**, *149*, 111587. DOI
59. Li, H.; Cao, L.; Wang, F.; et al. Fatsia japonica-derived hierarchical porous carbon for supercapacitors with high energy density and long cycle life. *Front. Chem.* **2020**, *8*, 89. DOI PubMed PMC
60. Sun, Y.; Li, X.; Sun, J.; Ren, Z. Molten salt-mediated hierarchical porous carbon derived from biomass waste for high-performance capacitive storage. *J. Power. Sources.* **2024**, *618*, 235216. DOI
61. Meng, X.; Zhang, D.; Wang, B.; et al. Biomass-derived phosphorus-doped hierarchical porous carbon fabricated by microwave irritation under ambient atmosphere with high supercapacitance performance in trifluoroacetic acid electrolyte. *J. Energy. Storage.* **2023**, *57*, 106345. DOI
62. Xia, C.; Surendran, S.; Ji, S.; et al. A sulfur self-doped multifunctional biochar catalyst for overall water splitting and a supercapacitor from Camellia japonica flowers. *Carbon. Energy.* **2022**, *4*, 491-505. DOI